The assembly of osmoDroplet reveals dehydration sensing by helix transition and association

Jingjing Zhang[1,2,5], Panting Fan[1,2,5], Xuebo Quan[3,5], Yahui Zhao[1,2], Lefei Gao[1,2], Jingyi Zhang[1,2], Xiaofeng Fang[4], Kai Huang[3*] & Shengbo He[1,2*]

[1]Guangdong Basic Research Center of Excellence for Precise Breeding of Future Crops, Guangdong Laboratory for Lingnan Modern Agriculture, College of Agriculture, South China Agricultural University, Guangzhou 510642, China.

[2]Key Laboratory for Enhancing Resource Use Efficiency of Crops in South China, Ministry of Agriculture and Rural Affairs, South China Agricultural University, Guangzhou 510642, Guangdong, China

[3]Institute of Systems and Physical Biology, Shenzhen Bay Laboratory, Shenzhen, Guangdong, China.

[4]Center for Plant Biology, School of Life Sciences, Tsinghua University, Beijing, 100084, China.

[5]These authors contributed equally: Jingjing Zhang, Panting Fan, Xuebo Quan.

[*]e-mail: huangkai@szbl.ac.cn; shengbo.he@scau.edu.cn

Abstract

Hyperosmotic stress triggers cellular dehydration and macromolecular crowding, leading to rapid biomolecular condensation. However, the individual roles of dehydration and crowding have been unclear, and the design principles of osmosensors remain poorly understood. Here, we identify a conserved sensor module comprising an osmo-sensing α-helix adjacent to an intrinsically disordered region (IDR). Using helices from Arabidopsis SEUSS and rice DRG9, we demonstrate that tandem repeats (≥2) self-assemble into a stable core that nucleates IDR condensation into 'osmoDroplets' in yeast under hyperosmotic stress. This assembly is tunable by helix copy number and IDR properties. The helices are largely unstructured under isotonic conditions but fold into stable α-helices upon hyperosmotic stress. Circular dichroism shows that dehydration specifically triggers this folding. Mutagenesis reveals that hydrophilic residues are essential for osmo-sensing, mediating changes in secondary structure and condensate formation. Simulations indicate that hyperosmolarity induces helical transition by reducing water-residue hydrogen bonds, compensated by intramolecular bonding. This versatile helix-IDR architecture functions across plant lineages and IDRs, defining a module where dehydration-driven folding directly transduces water loss into condensate assembly. Our work elucidates fundamental principles for engineering synthetic biological sensors and provides a practical tool for assessing the phase-separation capability of any given IDR.

Cells are constantly challenged by environmental fluctuations, and the ability to sense and respond to osmotic stress is central to cellular resilience[1–3]. Hyperosmotic conditions trigger rapid efflux of water, causing cellular dehydration, cytoplasmic shrinkage, and increased macromolecular crowding[1,4]. For sessile organisms such as plants, recurring exposure to drought or high salinity imposes strong selective pressure to evolve highly sensitive dehydration sensors and rapid adaptive mechanisms[4,5].

Over the past decade, liquid-liquid phase separation (LLPS) has emerged as a key mechanism by which cells reorganize molecular components under stress[6]. LLPS underlies the formation of membraneless biomolecular condensates that dynamically compartmentalize biochemical reactions[7–11]. A recurring theme in condensate biology is the synergy between structured self-associating scaffolds/cores and intrinsically disordered regions (IDRs): scaffolds/cores often provide binding surfaces or multivalent interaction hubs, while IDRs contribute the weak, transient interactions required for condensation[12,13]. Because IDRs alone usually need to reach unphysiologically high concentrations to phase separate, scaffolds are critical in lowering this threshold and nucleating condensates under physiological conditions. For example, the optoDroplet system, which couples the *Arabidopsis thaliana* CRY2 photolyase homology region (PHR) domain as a light-switchable oligomerizing scaffold to IDRs, enables optogenetic control of condensation and has become a versatile tool for probing LLPS and chromatin organization[12,14]. Such synthetic modules highlight the potential of engineering scaffold-based sensors that connect specific environmental cues to condensate formation[13,15]. However, how to design such synthetic sensors for diverse environmental signals remains to be investigated.

An increasing number of natural condensates likewise function as environmental sensors, responding to light, temperature, pH, redox state, or hydration levels[6,9,16–28]. In plants, stress-induced condensates are particularly critical for osmotic adjustment and signaling[25,26,29]. The Arabidopsis transcriptional coregulator SEUSS (SEU) and the rice DROUGHT RESISTANCE GENE 9 (DRG9), a double-stranded RNA binding protein, exemplify this principle. Upon hyperosmotic stress, SEU assembles into condensates that reprogram the transcriptome to promote cellular rehydration and survival[25], while DRG9 enhances drought tolerance in rice by undergoing stress-associated phase separation and partitioning into stress granules to safeguard

mRNA[29]. Both SEU and DRG9 harbor a specialized helix that is essential for hyperosmolarity-induced condensation of adjacent IDRs, suggesting that the osmo-sensing helix may act as the conditional scaffold coupling hyperosmolarity-induced conformational changes to condensate assembly. Their conservation from dicots to monocots and basal land plants points to an ancient helix-IDR osmosensing module[25]. However, the mechanisms underlying osmo-sensing of the specialized helix remain unclear.

Current models of hyperosmotic stress emphasize two main physical consequences: macromolecular crowding and dehydration. Crowding promotes macromolecular clustering, but acts relatively indiscriminately[30,31]. By contrast, dehydration directly perturbs protein hydration shells and strengthens intra- and intermolecular hydrogen bonding, thereby promoting specific conformational switching in vulnerable regions[32–35]. Although crowding has long been considered the dominant driver of hyperosmotic stress-induced condensation[25,26,28,30], mounting evidence supports dehydration as a distinct and often more specific determinant of osmotic sensing[36,37]. Yet, how dehydration-driven transitions are encoded in protein sequence and structure remains an open question.

Here, we investigate helix-IDR modules from SEU and DRG9 to dissect their role in osmo-responsive phase separation. We demonstrate that surface-exposed helices enriched in highly hydrophilic residues fold upon dehydration, undergo intermolecular association, and act as scaffolds that nucleate IDR condensation, giving rise to stress-inducible osmoDroplets. By integrating mutational analysis, live-cell imaging, biophysical assays, and molecular dynamics simulations, we uncover a conserved mechanism by which dehydration-induced helix folding and association scaffold IDR-driven condensation.

Results

SEU-helix and IDR fusion acts as an osmoDroplet module

AlphaFold3 predicts that the osmo-sensing helices in AtSEU and OsDRG9 are surface-exposed and exhibit relatively low helical propensity compared to more stable helices within the same proteins (plDDT<70 for SEU-helix, plDDT<90 for DRG9-helix vs. plDDT>90 for stable helices; Fig. 1a), suggesting the possibility of conditional helix formation. Both proteins share a helix-IDR module (Fig. 1a), which

we propose functions as a common hyperosmotic sensing module (designated osmoDroplet, Fig. 1b). In this module, the specialized helix serves as the osmo-sensing unit and IDR drives condensation. To test this, we first assessed a single SEU-helix copy fused to FUS-IDR (a commonly used IDR from ALS-related FUS protein[38]) under hyperosmotic stress in yeast using mVenus-tagged constructs (Fig. 1b). No fluorescent puncta formed for 1×helix^{SEU}-FUS^{IDR}-mVenus under sorbitol or NaCl treatments (Fig. 1c and Supplementary Fig. 1a), indicating a single helix and FUS-IDR fusion is insufficient for osmoDroplet assembly.

Tandem repeats of SEU-helix (2–3 copies) were then tested. While 2×helix^{SEU}-FUS^{IDR}-mVenus showed diffuse distribution in the untreated control conditions, 3 copies spontaneously condensed (Fig. 1c and Supplementary Fig. 1a). Under mild hyperosmotic stress (0.3 M NaCl or 0.6 M sorbitol), the 2-copy construct formed puncta in some cells; this intensified under severe stress (0.6 M NaCl or 1.2 M sorbitol; Fig. 1c and Supplementary Fig. 1a), confirming that two helices suffice to drive IDR condensation. The 3-copy fusion (3×helix^{SEU}-FUS^{IDR}-mVenus, termed osmoFUS^{SEU}) exhibited basal condensation in control conditions and the condensation was dramatically enhanced under both mild and severe stresses, with maximal puncta being formed under severe stress (Fig. 1c and Supplementary Fig. 1a). By contrast, 3×helix^{SEU}-mVenus (lacking FUS-IDR) showed minimal response to mild stress and weak condensation under severe stress (Fig. 1d and Supplementary Fig. 1b), indicating that both the helical scaffold and a “sticky” IDR are required for sensitive osmoDroplet assembly.

Helix-IDR represents a common osmoDroplet module

Previous studies have shown that SEU homologs across diverse species, ranging from bryophytes to angiosperms, contain osmo-sensing helices[25]. To test their functional conservation as scaffolds for osmoDroplet assembly, SEU-derived helices from representative species spanning all major clades were evaluated. Strikingly, all tested helices—when arranged as three tandem copies—triggered condensation of FUS-IDR under hyperosmotic stress, though with varying sensitivities (Supplementary Fig. 1c).

To generalize these findings, diverse IDRs from well-documented phase-separating proteins including TAF15, H2B.8, and SERRATE (SE)[39–41] were fused to 3×helix^{SEU}. All formed condensates under hyperosmotic stress but with varying efficiencies:

osmoTAF^{SEU} > osmoSE^{SEU} > osmoH2B.8^{SEU} (Fig. 1e), suggesting that IDRs fine tune condensation capacity of osmoDroplets.

We further examined the osmo-sensing helix of DRG9 (Fig. 1a), a drought-inducible phase-separating protein from rice[29]. Similar to SEU-helix, the fusion of three tandem DRG9-helix to FUS-IDR (osmoFUS^{DRG9}) formed condensates upon NaCl induction. By contrast, 3×helix^{DRG9} (lacking FUS- IDR) formed only sparse puncta (Fig. 1f).

Collectively, these results demonstrate that the helix–IDR represents a common osmoDroplet module, in which the helix enables osmo-sensing and IDRs fine tune condensation capacity.

Highly hydrophilic residues are essential for osmoDroplet assembly

We next investigated the sequence determinants underlying the hyperosmotic sensitivity of SEU- and DRG9-helices. Since both helices were capable of driving osmoDroplet assembly (Fig. 1c–f), we hypothesized that shared sequence features might form the basis of their osmo-sensing activity. Whereas SEU proteins are broadly conserved across land plants from bryophytes to angiosperms, DRG9 proteins are restricted to monocots[25,29]. Sequence analysis revealed glutamine (Q) enrichment in SEU-helices but not in DRG9-helices from representative species (Supplementary Fig. 2a, b), suggesting that Q enrichment is not a defining osmo-sensing feature. Supporting this, substituting Q with asparagine (N)—an amino acid of comparable hydrophilicity (M1 variant; Fig. 2a, c)—preserved helical propensity (Supplementary Fig. 2c) and retained robust puncta formation under hyperosmotic stress (Fig. 2d). These results indicate that Q enrichment is dispensable for osmo-sensing and instead point to strong hydrophilicity as the critical determinant, as reduced free water availability under hyperosmotic conditions likely influences the conditional formation of metastable helices.

Charged residues (Asp, Glu, Arg, Lys, His) and strongly polar residues (Gln, Asn) exhibit high hydrophilicity due to their capacity for strong ion-dipole interactions and hydrogen bonding with water. Weakly polar residues (Ser, Thr, Tyr) show moderate hydrophilicity, while nonpolar residues (e.g., Leu, Ile, Val) are hydrophobic (Fig. 2a). SEU and DRG9 helices across diverse species are surface-exposed and contain substantial numbers of highly hydrophilic residues, with SEU-helices having around 50% strongly polar residues and DRG9-helices containing about 33% charged

residues (Fig. 1a and Supplementary Fig. 2d). To place these helices in a broader structural context, we extracted all helices from experimentally validated protein structures stored in the PDB (Protein Data Bank). After removing hydrophobic and redundant entries, 13,878 non-redundant helices from 8,972 proteins were retained for analysis. Kernel density estimation (KDE) in a ternary plot revealed that SEU-helices clustered near the strongly polar vertex (bottom left), while DRG9-helices shifted toward the charged-residue vertex (top), both diverging significantly from the bulk helices (Fig. 2b; Kolmogorov-Smirnov test, p=8.103e-33 for SEU-helices and p=1.732e-03 for DRG9-helices). This demonstrates that SEU-helices and DRG9-helices are enriched with strongly polar and charged residues, respectively. The high hydrophilicity of charged and strongly polar residues indicates that SEU/DRG9-helices are exceptionally hydrophilic relative to typical helices.

To assess the role of hydrophilicity, we generated SEU-helix variants (M2–M7) by substituting highly hydrophilic residues with weakly hydrophilic or hydrophobic alternatives (Fig. 2c). All variants retained helical folding according to AlphaFold3 predictions (Supplementary Fig. 2c). Nonetheless, condensation activity was markedly reduced in M2 (Q→S/T), completely abolished in M3 (Q→S/T/Y), strongly attenuated in M4 (Q→11 Leu), and fully eliminated in M5 (Q/N/E→14 Leu), M6 (Q→12 Tyr), and M7 (Q/N/H/E/R→14 Tyr; Fig. 2c–e). These results demonstrate that the high hydrophilicity provided by charged and strongly polar residues is essential for helix-driven IDR condensation in response to hyperosmotic stress.

Conformational response to hyperosmolarity requires highly hydrophilic residues

SEU-IDR1, which contains the SEU-helix, undergoes hyperosmolarity-induced conformational changes from an open to a closed state[25]. To test whether the SEU-helix alone is sufficient for this response, we fused mTurquoise2 (donor) and mNeonGreen (acceptor) to a single SEU-helix for FRET (Fluorescence Resonance Energy Transfer) assays (Fig. 2f). As expected, hyperosmotic stress significantly increased FRET efficiency, reflected by an elevated mNeonGreen/mTurquoise2 fluorescence ratio relative to the untreated control (Fig. 2g), confirming a conformational change. This response was diminished by substitutions in the M4 variant and completely abolished in the M5–M7 variants (Fig. 2c, g), consistent with

their impaired ability to drive IDR condensation (Fig. 2e). Together, these findings underscore the critical role of hydrophilic residues in enabling conformational osmo-sensing.

Dehydration induces helix folding

Surface-exposed osmo-sensing helices inevitably have contacts with surrounding water molecules, yet their low AlphaFold3 confidence scores suggest that their structures are environmentally dependent (Fig. 1a). Hyperosmotic stress simultaneously imposes dehydration and macromolecular crowding, which are difficult to disentangle in vivo. To separate these effects in vitro, we used increasing concentrations (up to 80%) of ethylene glycol (EG) to mimic dehydration and moderate concentrations (not higher than 10%) of polyethylene glycol (PEG) to mimic crowding. Circular dichroism (CD) measurements of synthetic SEU-helix1, SEU-helix2, and DRG9-helix peptides revealed low basal helicity under control conditions (Fig. 3a–g), consistent with their predicted instability (Fig. 1a). Addition of EG increased helicity in a concentration-dependent manner: SEU-helix1 rose from 14.5% (control) to 29.2% (80% EG; Fig. 3b, c), SEU-helix2 from 15.6% to 61.8% (Fig. 3d, e), and DRG9-helix displayed a sharp folding transition approaching near-saturation (Fig. 3f, g). By contrast, up to 10% PEG6000 produced only marginal changes in helical content (Supplementary Fig. 3a–f). These findings indicate that dehydration specifically promotes helix folding in hydrophilic-rich peptides, thereby providing a mechanistic basis for their osmo-sensing properties.

To assess the contribution of high hydrophilicity to helix transition, we performed CD assays on synthetic SEU-helix2 peptides containing mutations where key hydrophilic residues were replaced with less polar or hydrophobic ones (Fig. 2c). The results show that these variants maintained a basal level of helicity and failed to undergo enhanced helix transition upon EG treatment (Supplementary Fig. 4). This demonstrates that highly hydrophilic residues are essential for dehydration-induced helix transition. Since the same mutations attenuated or abolished the hyperosmotic stress response in conformation and assembly (Fig. 2c–g), these findings strongly suggest that helix transition is the immediate molecular event, preceding downstream conformational changes and condensate assembly.

Dehydration induces intra-molecular hydrogen bonding of SEU/DRG9-helices by

molecular dynamics simulation

For SEU-helix1 and DRG9-helix, we quantitatively analyzed the variation of their helical contents by molecular dynamics (MD) simulation in water and 60% EG, respectively. The simulation results show that, compared with water, the helical contents for both SEU-helix1 and DRG9-helix in EG are more stable and higher (Fig. 4a, b, e, f and Supplementary Movies 1-4), which is in good agreement with CD results (Fig. 3b, c, f, g). To further uncover the underlying biophysics mechanism, we computed the number of inter-residue and water-residue hydrogen bonds (H-bonds). It shows that the number of inter-residue H-bonds in EG is significantly higher than in water (Fig. 4c, g), whereas the number of H-bonds between residues and water molecules is lower in EG (Fig. 4d, h). This behavior can be rationalized by the strong H-bonding ability of EG molecules with water molecules, which reduces water accessibility for residues. Consequently, EG effectively promotes the stabilization of protein secondary structure, particularly α-helix, by favoring inter-residue H-bonding over protein–solvent interactions.

SEU/DRG9-helices undergo hyperosmolarity-enhanced intermolecular association

Multimerization of modular domains through self-association can act as a scaffold or core for nucleating IDR condensation[12,13]. To elucidate the scaffolding mechanism of the helices, we performed yeast 2-hybrid (Y2H) assay and found that 3×helix^{SEU} self-associates, enabling yeast growth on selective medium under normal osmolarity (Fig. 5a), consistent with the basal osmoFUS^{SEU} condensation in the absence of hyperosmotic stress (Fig. 1c, d). Hyperosmotic stress inhibited yeast growth, so we employed FRET to directly probe hyperosmolarity-enhanced helix interactions. When fused to mTurquoise2 and mNeonGreen, 3×helix^{SEU} fusions colocalized under hyperosmotic treatment (Fig. 5b). Similar colocalization was observed for 3×helix^{DRG9} fusions, particularly under hyperosmotic treatment (Fig. 5c). Moreover, hyperosmotic stress significantly increased FRET efficiency, reflected by elevated mNeonGreen/mTurquoise2 ratios, for both 3×helix^{SEU} and 3×helix^{DRG9} compared to untreated controls (Fig. 5d, e). By contrast, the group 4 Late Embryogenesis Abundant protein (LEA4- 5), which undergoes helix transitions and conformational changes under hyperosmotic stress[36,37], showed no self- interaction in either Y2H or FRET

assays (Supplementary Fig. 5a, b). Consequently, three tandem repeats of LEA helices failed to scaffold IDR condensation (Supplementary Fig. 5c). Taken together, these results demonstrate that SEU and DRG9 helices undergo hyperosmolarity-enhanced intermolecular association, which in turn scaffolds IDR condensation.

Hydration dynamics across distinct conformational states of SEU-helix by MD simulation

We systematically investigated the dynamic behavior of the SEU-helix in 60% EG across four distinct conformational states (state A-disorder, state B-open helix, state C-closed helix and state D-stable core via self-association), as depicted in Fig. 6a-d. We quantified the number of inter-residue and water-residue H-bonds for the four protein states (Fig. 6e, f). The results show that the number of inter-residue H-bonds increased steadily from state A to state D (Fig. 6e), whereas the number of water-residue decreased accordingly (Fig. 6f). Notably, the transition from state A to state B exhibited the most pronounced change, highlighting that alterations in H-bonding interactions are a key driving force underlying the conformational switch from a disordered ensemble to a helical state. To gain further insight into the hydration structure and the organization of water around proteins, we computed the radial distribution function (g(r)) of water molecules relative to the protein. As shown in Fig. 6g-j, the first peak in g(r) profiles located near 0.3 nm denotes the immediate hydration shell, which displays the highest intensity as indicated by the highest g(r) value in state A among the four states. This indicates that state A maintains the strongest hydration shell, which is weakening in states B-D, in agreement with the water-residue analysis (Fig. 6f).

Discussion

We elucidate a conserved molecular mechanism wherein dehydration-induced helix folding drives biomolecular condensation via tunable helix-IDR modules (Fig. 7). Metastable helices enriched with highly hydrophilic residues act as conformational switches: dehydration reduces the strong hydration shell of unstructured polypeptides (mediated by residue-water H-bonds; *State A*), thereby strengthening residue-residue H-bonds to form transient open helices (*State B*). The open helix further folds into a closed conformation stabilized by inter-helix H-bonds (*State C*). Subsequently, closed helices undergo inter-molecular association via H-bond interactions (*State D*),

297 forming a stable core for scaffolding IDR condensation.

298 The hydration of hydrophilic residues is a key driver of protein folding and
299 association. Perturbing this hydration shell—through dehydration by ethylene glycol
300 or by hyperosmotic stress—fundamentally alters the protein's solvation
301 microenvironment, likely by reducing micropolarity. Given the emerging importance
302 of micropolarity in regulating phase separation and ligand partitioning[42,43], we
303 propose that highly hydrophilic residues may function as sensors for these changes.
304 This mechanism offers a novel hypothesis for cellular hyperosmotic sensing and
305 warrants further investigation. Nonetheless, highly hydrophilic residues alone are
306 insufficient for scaffolding IDR condensation, as demonstrated by the failure of
307 LEA4-helix to drive IDR condensation (Supplementary Fig. 5c). Helical
308 self-association is additionally required to establish a stable scaffold for nucleating
309 IDR condensation (Fig. 5).

310 Functionally conserved helices in bryophytes and angiosperms suggest an ancient
311 stress-adaptation strategy for terrestrial drought survival[44,45]. Hydrophilic residue
312 conservation reflects strong selective pressure for dehydration sensitivity, while IDR
313 identity tunes condensation efficiency, enabling evolutionary flexibility in stress
314 response kinetics.

315 This study highlights dehydration effects on helix folding, conformational changes,
316 helical self-association, and osmoDroplet assembly. This contrasts with molecular
317 crowding effects—a common focus in the field[25,26,28]. While crowding—a
318 consequence of hyperosmotic stress—can promote conformational shifts in tertiary
319 structure (e.g., SEU and DCP5)[25,26], dehydration sensing operates distinctly. Crowding
320 agents like PEG enhance phase separation in vitro likely by increasing the frequencies
321 of molecular collision but with little specificity—PEG appears to be a general
322 enhancer of in vitro phase separation; thus, defining sensors for crowding effects
323 requires additional evidence (e.g., crowding-induced conformational changes via
324 FRET, as in SEU and DCP5)[25,26]. Here, dehydration induces helix folding in both
325 SEU-helix and DRG9-helix, underscoring the role of highly hydrophilic residues in
326 secondary-structural sensing. This distinguishes dehydration-driven responses
327 (secondary structure) from crowding-driven effects (tertiary structure) in osmosensors.
328 Hydrophobic residues may mediate crowding sensitivity as shown in the case of

DCP5 osmosensor[26], whereas strong hydrophilicity confers dehydration sensitivity.

One application of our system is that the SEU/DRG9-helix module can be used to assess whether a given IDR is capable of undergoing phase separation. By fusing the IDR of interest to SEU/DRG9-helix, phase separation behavior can be examined in yeast cells under both control and hyperosmotic conditions. While the optoIDR system has been widely employed for this purpose, it requires specialized light illumination equipment[12]. In contrast, our osmoIDR system is equally effective yet far more accessible, as it relies solely on the addition of common chemicals such as NaCl or sorbitol to induce hyperosmotic stress.

In addition, the helix-IDR module proposed for osmoDroplet assembly offers a design paradigm for engineering synthetic condensates that respond to specific environmental signals. The strategy involves identifying a minimal environmental sensing unit from a native sensor protein. Provided this unit also self-associates into a nucleating core, it can be harnessed to drive condensation of various IDRs, hence the assembly of environmentally responsive synthetic condensates. This approach is particularly powerful given the growing number of identified environmental sensors—such as sensors responsive to high or low temperatures (e.g., ELF3, TWA1, FUST1, FRI)[18–21] and redox states (e.g., TMF)[27]—that drive phase separation. Expanding the repertoire of synthetic condensates will further enrich the toolbox of condensate biology, enhancing crop performance and resilience in the face of an ever- changing climate.

Methods

DNA constructs

To generate the constructs for visualizing osmoDroplet in yeast cells, the fragments of $n \times \text{helix}^{\text{SEU/DRG9}}$ with or without FUS^{IDR} as well as all the $\text{helix}^{\text{SEU}}$ variants were amplified and inserted into the pAV0751 vector[46]. For osmoTAF$^{\text{SEU}}$, osmoSE$^{\text{SEU}}$, and osmoH2B.8$^{\text{SEU}}$ constructs, the FUS^{IDR} in the osmoFUS$^{\text{SEU}}$ construct was substituted with distinct IDRs.

For probing conformational changes of SEU-helix and the variants, FRET constructs were generated by fusing mNeonGreen[47], WT/M1-7 SEU-helix mutants, and mTurquoise2 into a single cassette in the backbone of pAV0751 for yeast expression.

To study protein-protein interactions by FRET, DNA fragments encoding 3×helix$^{SEU/DRG9/LEA}$ fused to mTurquoise2 or mNeonGreen were cloned into pSH0612 (a vector modified from pAV0612 with the *nmt1* inducible promoter replaced with the *tdh1* constitutive promoter) or pAV0751, respectively[46]. For yeast two-hybrid assays, 3×helix$^{SEU/LEA}$ were subcloned into bait (pGBKT7) and prey (pGADT7) vectors, respectively.

Fission yeast expression

The LD330 strain (genotype his- ura4-D18)[46] was revived on YES solid medium using the streak-plate method and incubated at 28℃ for 2-3 days. Individual colonies were then transferred to YES liquid medium and pre-cultured overnight at 28℃ with 220-rpm orbital shaking. The overnight cultures were 1:100 diluted in YES liquid medium and grown at 28℃ for 4–6 hours with optical density at 600 nm (OD600) reaching within 0.1-0.2. Prior to transformation, plasmids were linearized using PmeI and AflII restriction enzymes. Yeast cells were harvested at mid-logarithmic growth phase (OD600=0.4-0.8), washed twice with sterile water, and finally resuspended in an appropriate buffer (240 µl of 50% PEG4000 (w/v), 36 µl of LiAc (1.0 M), 10 µl of boiled single-stranded carrier DNA (10 mg/ml), 34 µl of the linearized plasmids (up to 1000 ng) and 40 µl sterile water). Samples were vortex-mixed, incubated at 42℃ for 40 min, and immediately chilled on ice for 3 min. After adding 500 µl of YES liquid medium, cultures were revived in a 28℃ orbital shaker (220 rpm) for 30 min. Cell pellets were washed, resuspended in 300 µl sterile water, and plated onto uracil-deficient Edinburgh Minimal Medium (EMM-Ura) agar plates for 3-4 days of incubation at 28℃.

Microscopy

For live-cell imaging of yeast cells, colonies grown on agar plates were inoculated into liquid medium and revived overnight under optimal culture conditions. Cells from each treatment group were pelleted by centrifugation and resuspended in 20 µl of liquid medium supplemented with or without sorbitol and NaCl for 5 min. Cell suspensions were spotted onto glass slides and mounted with coverslips. For control samples, a low-concentration agarose solution was overlaid to prevent dehydration, followed by sealing with fixative around the coverslip edges to minimize mechanical displacement. Confocal imaging was performed using a Leica SP8 laser confocal

392 microscope. The mVenus fluorescent protein was excited at 514 nm, with emitted
393 fluorescence captured within a 517-557 nm detection window. Image acquisition was
394 conducted under a 63×/1.40 NA oil immersion objective.

395 **Förster resonance energy transfer analyses**

396 FRET experiments were performed essentially as described[25]. Briefly, FRET
397 measurements were conducted on a Leica TCS SP8 confocal microscope fitted with a
398 63×/1.40 NA oil-immersion objective. Fluorescence emission spectra were acquired
399 from 460 to 570 nm (9.09-nm step size) with 448-nm excitation and a spectral
400 bandwidth of 10 nm. FRET efficiencies were measured by mNeonGreen (514 nm) /
401 mTurquoise2 (469 nm) fluorescence ratios using Leica acquisition software. At least
402 30 yeast cells were analyzed for each condition.

403 **Circular dichroism (CD) spectroscopy**

404 The SEU-helix1, SEU-helix2, and DRG9-helix peptides were diluted in 10 mM
405 phosphate buffer (pH 8.0), either with or without ethylene glycol (EG; 20-80% v/v) or
406 PEG6000 (2-10% w/v). CD spectra of peptide mixtures were acquired on a
407 Chirascan™ spectrometer (Applied Photophysics Ltd), using a 0.5-mm pathlength
408 quartz cuvette. Three consecutive spectral scans were acquired per sample preparation,
409 averaged, and smoothed using a noise-reduction algorithm. Circular dichroism (CD)
410 spectra, expressed in millidegrees (mdeg), were processed using the CDNN algorithm
411 for computing secondary structures.

412 **Yeast two-hybrid assays**

413 AD and BD plasmids were cotransformed into the Y2HGold yeast strain. Following
414 the addition of 10 µl denatured carrier DNA (boiled and ice-chilled) and 500 µl
415 PEG/LiAc solution, samples were mixed by gentle flicking every 10 minutes and
416 incubated in a 30°C water bath for 30 minutes with additional mixing at 15 minutes.
417 Tubes were incubated in a 42°C water bath for 15 minutes, with gentle inversion
418 performed at 7.5 minutes to homogenize the contents. Samples were centrifuged at
419 5,000×g for 40 seconds to pellet cellular components, followed by supernatant
420 removal. Pellets were resuspended in 400 µl of ddH_2O, and centrifuged again at
421 5,000×g for 30 seconds. After discarding the supernatant, the final pellet was
422 resuspended in 50 µl of ddH_2O and plated onto SD/-Trp/-Leu synthetic defined

medium, followed by incubation at 28°C for 2-3 days. More than three single colonies were selected, resuspended in sterile water, and subjected to serial dilutions. Aliquots were spotted onto synthetic defined media: SD/-Trp/-Leu, SD/-His/-Trp/-Leu, and SD/-Trp/-Leu/-Ade/-His, followed by incubation at 28°C for 2-3 days to assess growth phenotypes.

Analysis of sequence features in alpha-helices

This study was based on a dataset derived from the RCSB Protein Data Bank (PDB, https://www.rcsb.org/). We selected all experimentally validated 71,141 protein structures that contain α-helical regions and had a resolution higher than 3.0 Å. From these structures, all alpha-helical sequences with a length exceeding 20 residues but hydrophobic helices (with a percentage of hydrophobic residues > 70%) were extracted. To construct a non-redundant dataset for analysis, the extracted sequences were clustered using the MMseqs2 (v13.45111) software[48] suite (--cov-mode 0 --min-seq-id 0.8 --cluster-mode 2) and unique sequences were retained. Finally, we calculated the compositional proportion of each of the three residue types (charged, strongly polar, and weakly polar) within the resulting alpha-helical sequences. The distribution patterns of these compositions were statistically analyzed and visualized using Kernel Density Estimation (KDE), which was implemented with the scipy.stats[49] and matplotlib[50] libraries in Python.

Molecular dynamics simulation

The SEU-helix1 and DRG9-helix were first simulated in water and 60% EG solution. The initial atomic models were predicted by the Alphafold2 program[51]. The protein chains were placed in a periodic rectangle simulation box of dimensions of 7×7×7 nm^3 solvated with water molecules, and appropriate number of counter-ions were added to neutralize the protein systems. The CHARMM36m all-atom force field[52] was used to describe proteins and EG molecule, and the TIP3P model was used for water molecules. The protein systems were first energy minimized with 5000 steps and then equilibrated for 1 ns under the NVT and NPT ensemble, respectively, with protein heavy atoms restrained during simulations. Finally, 5 μs production run was conducted with protein restraints released. In addition, four different states (disordered, open-helix, closed-helix and stable core) of SEU-helix in 60% EG

solution were simulated, and three independent 10 ns production runs were performed for each protein state. All simulations were performed with the GROMACS 2023 package[53]. The long-range electrostatic interactions were calculated by the Particle Mesh Ewald (PME) method with a cutoff radius of 1 nm. Van der Waals interactions were calculated using a cutoff of 1 nm. The temperature was maintained at 300 K by the V-rescale method, and the pressure was maintained at 1 bar by the Parrinello-Rahman coupling method. The equations of motion were integrated using a leap-frog algorithm with a time step of 2 fs. 3D periodic boundary conditions were applied to all the simulations.

The dynamic behavior of proteins in water and EG solution was characterized by helix content, protein-protein and protein-water hydrogen bonds. All trajectory analyses were accomplished using our in house developed scripts and tools implemented in the GROMACS and MDTraj packages[54]. The secondary structures of proteins were determined by the DSSP program[55]. For structural visualization, the Visual Molecular Dynamics (VMD)[56] program was used.

References

1. Bremer, E. & Krämer, R. Responses of Microorganisms to Osmotic Stress. *Annu. Rev. Microbiol.* **73**, 313–334 (2019).
2. Zhang, H., Zhu, J., Gong, Z. & Zhu, J.-K. Abiotic stress responses in plants. *Nat. Rev. Genet.* **23**, 104–119 (2022).
3. Lang, F. *et al.* Functional Significance of Cell Volume Regulatory Mechanisms. *Physiol. Rev.* **78**, 247–306 (1998).
4. Yu, B., Chao, D. & Zhao, Y. How plants sense and respond to osmotic stress. *J. Integr. Plant Biol.* **66**, 394–423 (2024).
5. Hasegawa, P. M., Bressan, R. A., Zhu, J.-K. & Bohnert, H. J. PLANT CELLULAR AND MOLECULAR RESPONSES TO HIGH SALINITY. *Annu. Rev. Plant. Physiol. Plant. Mol. Biol.* **51**, 463–499 (2000).
6. Peng, J., Yu, Y. & Fang, X. Stress sensing and response through biomolecular condensates in plants. *Plant Commun.* **6**, 101225 (2025).
7. Xu, X., Zheng, C., Lu, D., Song, C. & Zhang, L. Phase separation in plants: New insights into cellular compartmentalization. *J. Integr. Plant Biol.* **63**, 1835–1855 (2021).
8. Liu, Q., Liu, W., Niu, Y., Wang, T. & Dong, J. Liquid–liquid phase separation in plants: Advances and perspectives from model species to crops. *Plant Commun.* **5**, 100663 (2023).
9. Fan, P. *et al.* Exploring the frontier of plant phase separation: Current insights and future prospects. *New Crops* **1**, 100026 (2024).
10. Banani, S. F., Lee, H. O., Hyman, A. A. & Rosen, M. K. Biomolecular condensates:

organizers of cellular biochemistry. *Nat. Rev. Mol. Cell Biol.* **18**, 285–298 (2017).

11. Shin, Y. & Brangwynne, C. P. Liquid phase condensation in cell physiology and disease. *Science* **357**, eaaf4382 (2017).
12. Shin, Y. *et al.* Spatiotemporal Control of Intracellular Phase Transitions Using Light-Activated optoDroplets. *Cell* **168**, 159–171 (2017).
13. Wan, L., Ke, J., Zhu, Y., Zhang, W. & Mu, W. Recent advances in engineering synthetic biomolecular condensates. *Biotechnol. Adv.* **77**, 108452 (2024).
14. Shin, Y. *et al.* Liquid Nuclear Condensates Mechanically Sense and Restructure the Genome. *Cell* **175**, 1481–1491 (2018).
15. Hilditch, A. T. *et al.* Assembling membraneless organelles from de novo designed proteins. *Nat. Chem.* **16**, 89–97 (2024).
16. Jiang, B. *et al.* Light-induced LLPS of the CRY2/SPA1/FIO1 complex regulating mRNA methylation and chlorophyll homeostasis in Arabidopsis. *Nat. Plants* **9**, 2042–2058 (2023).
17. Mo, W. *et al.* Arabidopsis cryptochrome 2 forms photobodies with TCP22 under blue light and regulates the circadian clock. *Nat. Commun.* **13**, 2631 (2022).
18. Jung, J.-H. *et al.* A prion-like domain in ELF3 functions as a thermosensor in Arabidopsis. *Nature* **585**, 256–260 (2020).
19. Geng, P. A thermosensor FUST1 primes heat-induced stress granule formation via biomolecular condensation in Arabidopsis. *Cell Res.* **35**, 483–496 (2025).
20. Bohn, L. *et al.* The temperature sensor TWA1 is required for thermotolerance in Arabidopsis. *Nature* **629**, 1126–1132 (2024).
21. Zhu, P., Lister, C. & Dean, C. Cold-induced Arabidopsis FRIGIDA nuclear condensates for FLC repression. *Nature* **599**, 657–661 (2021).
22. Chen, D. *et al.* Integration of light and temperature sensing by liquid-liquid phase separation of phytochrome B. *Mol. Cell* **82**, 3015–3029 (2022).
23. Feng, Z. *et al.* Liquid–liquid phase separation of TZP promotes PPK-mediated phosphorylation of the phytochrome A photoreceptor. *Nat. Plants* **10**, 798–814 (2024).
24. Dorone, Y. *et al.* A prion-like protein regulator of seed germination undergoes hydration-dependent phase separation. *Cell* **184**, 4284–4298 (2021).
25. Wang, B. *et al.* Condensation of SEUSS promotes hyperosmotic stress tolerance in Arabidopsis. *Nat. Chem. Biol.* **18**, 1361–1369 (2022).
26. Wang, Z. *et al.* A cytoplasmic osmosensing mechanism mediated by molecular crowding–sensitive DCP5. *Science* **386**, eadk9067 (2024).
27. Huang, X. *et al.* ROS regulated reversible protein phase separation synchronizes plant flowering. *Nat. Chem. Biol.* **17**, 549–557 (2021).
28. Boyd-Shiwarski, C. R. *et al.* WNK kinases sense molecular crowding and rescue cell volume via phase separation. *Cell* **185**, 4488–4506 (2022).
29. Wang, H. *et al.* A double-stranded RNA binding protein enhances drought resistance via protein phase separation in rice. *Nat. Commun.* **15**, 2514 (2024).
30. Subramanya, A. R. & Boyd-Shiwarski, C. R. Molecular Crowding: Physiologic Sensing and Control. *Annu. Rev. Physiol.* **86**, 429–452 (2024).
31. Vweza, A.-O., Song, C.-G. & Chong, K.-T. Liquid–Liquid Phase Separation in the Presence of Macromolecular Crowding and State-dependent Kinetics. *Int. J. Mol. Sci.* **22**, 6675 (2021).
32. Loh, D. & Reiter, R. J. Light, Water, and Melatonin: The Synergistic Regulation of Phase

Separation in Dementia. *Int. J. Mol. Sci.* **24**, 5835 (2023).

33. Prestrelski, S. J., Tedeschi, N., Arakawa, T. & Carpenter, J. F. Dehydration-induced conformational transitions in proteins and their inhibition by stabilizers. *Biophys. J.* **65**, 661–671 (1993).
34. Fernández, A. & Scheraga, H. A. Insufficiently dehydrated hydrogen bonds as determinants of protein interactions. *Proc. Natl. Acad. Sci. U.S.A.* **100**, 113–118 (2003).
35. Mallamace, D., Fazio, E., Mallamace, F. & Corsaro, C. The Role of Hydrogen Bonding in the Folding/Unfolding Process of Hydrated Lysozyme: A Review of Recent NMR and FTIR Results. *Int. J. Mol. Sci.* **19**, 3825 (2018).
36. Cuevas-Velazquez, C. L., Saab-Rincón, G., Reyes, J. L. & Covarrubias, A. A. The Unstructured N-terminal Region of Arabidopsis Group 4 Late Embryogenesis Abundant (LEA) Proteins Is Required for Folding and for Chaperone-like Activity under Water Deficit. *J. Biol. Chem.* **291**, 10893–10903 (2016).
37. Rendón-Luna, D. F. *et al.* Alternative conformations of a group 4 Late Embryogenesis Abundant protein associated to its in vitro protective activity. *Sci. Rep.* **14**, 2770 (2024).
38. Dormann, D. & Haass, C. Fused in sarcoma (FUS): An oncogene goes awry in neurodegeneration. *Mol. Cell Neurosci.* **56**, 475–486 (2013).
39. Couthouis, J. *et al.* A yeast functional screen predicts new candidate ALS disease genes. *Proc. Natl. Acad. Sci. U.S.A.* **108**, 20881–20890 (2011).
40. Buttress, T. *et al.* Histone H2B.8 compacts flowering plant sperm through chromatin phase separation. *Nature* **611**, 614–622 (2022).
41. Xie, D. *et al.* Phase separation of SERRATE drives dicing body assembly and promotes miRNA processing in Arabidopsis. *Nat. Cell Biol.* **23**, 32–39 (2021).
42. Ye, S. *et al.* Micropolarity governs the structural organization of biomolecular condensates. *Nat. Chem. Biol.* **20**, 443–451 (2024).
43. Ouyang, J. *et al.* Navigating condensate micropolarity to enhance small-molecule drug targeting. *Nat. Chem. Biol.* https://www.nature.com/articles/s41589-025-02017-9 (2025).
44. Kunz, C. F., Goldbecker, E. S. & De Vries, J. Functional genomic perspectives on plant terrestrialization. *Trends Genet.* **41**, 617–629 (2025).
45. Cheng, S. *et al.* Genomes of Subaerial Zygnematophyceae Provide Insights into Land Plant Evolution. *Cell* **179**, 1057–1067 (2019).
46. Vještica, A. *et al.* A toolbox of stable integration vectors in the fission yeast *Schizosaccharomyces pombe*. *J. Cell Sci.* **133**, jcs240754 (2020).
47. Mastop, M. *et al.* Characterization of a spectrally diverse set of fluorescent proteins as FRET acceptors for mTurquoise2. *Sci. Rep.* **7**, 11999 (2017).
48. Steinegger, M. & Söding, J. MMseqs2 enables sensitive protein sequence searching for the analysis of massive data sets. *Nat. Biotechnol.* **35**, 1026–1028 (2017).
49. Virtanen, P. *et al.* SciPy 1.0: fundamental algorithms for scientific computing in Python. *Nat. Methods* **17**, 261–272 (2020).
50. Hunter, J. D. Matplotlib: A 2D Graphics Environment. *Comput. Sci. Eng.* **9**, 90–95 (2007).
51. Jumper, J. *et al.* Highly accurate protein structure prediction with AlphaFold. *Nature* **596**, 583–589 (2021).
52. Huang, J. *et al.* CHARMM36m: an improved force field for folded and intrinsically disordered proteins. *Nat. Methods* **14**, 71–73 (2017).

53. Hess, B., Kutzner, C., Van Der Spoel, D. & Lindahl, E. GROMACS 4: Algorithms for Highly Efficient, Load-Balanced, and Scalable Molecular Simulation. *J. Chem. Theory Comput.* **4**, 435–447 (2008).
54. McGibbon, R. T. *et al.* MDTraj: A Modern Open Library for the Analysis of Molecular Dynamics Trajectories. *Biophys. J.* **109**, 1528–1532 (2015).
55. Kabsch, W. & Sander, C. Dictionary of protein secondary structure: Pattern recognition of hydrogen-bonded and geometrical features. *Biopolymers* **22**, 2577–2637 (1983).
56. Humphrey, W., Dalke, A. & Schulten, K. VMD: Visual molecular dynamics. *J. Mol. Graph.* **14**, 33–38 (1996).

Acknowledgements

We thank Dr. Lilin Du from National Institute of Biological Sciences, Beijing, China for generously providing yeast constructs and strains used for fluorescence visualization. We thank Prof. Chengcai Chu and Prof. Bin Hu from South China Agricultural University for helpful discussions. This work was supported by the Biological Breeding-National Science and Technology Major Project (2023ZD04073), Guangdong Provincial Special Fund for Science and Technology Innovation Strategy (the Cultivation of Science and Technology Innovation in College Students, pdjh2024a071), Guangdong Provincial "Pearl River Talent Program" Innovation and Entrepreneurship Team Project (2023ZT10N019), Guangdong Basic Research Center of Excellence for Precise Breeding of Future Crops (FCBRCE-202513), National Natural Science Foundation of China (32370345, 32571445, 32521002), the Major Program of Shenzhen Bay Laboratory (S241101001), Guangdong Laboratory for Lingnan Modern Agriculture (NG2021005), Double first-class discipline promotion project of Guangdong province (2021B10564001), Natural Science Foundation of Guangdong province (2023A1515012067, 2024A1515010717), Guangzhou Science and Technology Elite "Navigator" Program (2024A04J3436), and Guangdong Provincial Pearl River Talent Plan (2021QN020536).

Author contributions

S.H. designed the study. J-J.Z., P.F., L.G. performed all experiments. X.Q, K.H., performed molecular dynamics simulations. Y.Z. performed sequence analyses. J-J.Z., P.F., X.Q., K.H., J-Y.Z, S.H. analyzed data. S.H., P.F., J-J.Z., X.Q., K.H., J-Y.Z., X.F. wrote and revised the article.

Competing interests

The authors declare no competing interests.

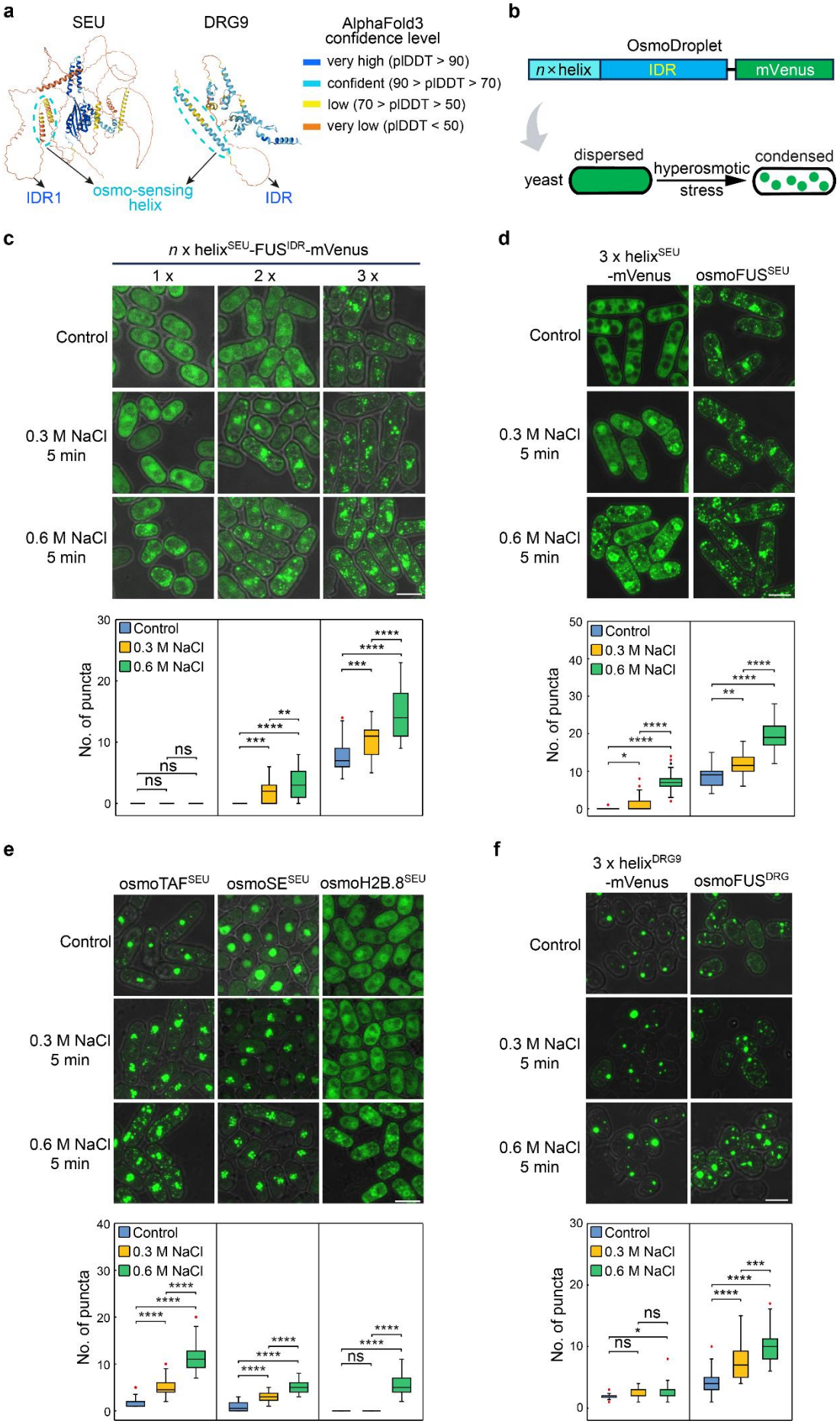

Fig. 1 Helix-IDR functions as a sensitive osmoDroplet module

(a) AlphaFold3-predicted structures of *Arabidopsis thaliana* SEU (left) and *Oryza sativa* DRG9 (right), with osmo-sensing α-helices (cyan) and intrinsically disordered regions (IDRs, blue) highlighted which were previously shown to mediate phase separation. Prediction confidence is color-coded (blue: very high; red: very low). plDDT (Predicted Local Distance Difference Test) is a per-residue confidence metric in AlphaFold3 that quantifies the model's reliability for predicting the local atomic structure around each residue.

(b) Schematic diagram of the osmoDroplet system in yeast, depicting phase transition from dispersed to condensed states in response to hyperosmotic stress.

(c-f) Confocal images (top panels) and corresponding quantitative analyses (bottom panels) of yeast cells exposed to control or NaCl treatments (0.3 M or 0.6 M, 5 min). Box plots quantified puncta formation per cell. Each box encloses the middle 50% of the distribution, with the horizontal line marking the median and the vertical lines marking the minimum and maximum values that fall within 1.5 times the height of the box. ns, not significant; ****$p < 0.0001$, ***$p < 0.001$, **$p < 0.01$, *$p < 0.05$ (one-way ANOVA followed by Tukey's HSD test; $n \geq 30$ cells per group). c: Yeast cells expressing different copies of SEU-helices fused to FUS-IDR and mVenus ($n = 1$, 2, 3). d: Yeast cells expressing 3 copies of SEU-helices with (osmoFUS^{SEU}) or without FUS-IDR fusion (3×helix^{SEU}). e: Yeast cells expressing 3 copies of SEU-helices fused to the indicated IDRs (TAF15-IDR, SE-IDR, H2B.8-IDR). SE, SERRATE. f: Yeast cells expressing 3 copies of DRG9-helices with (osmoFUS^{DRG9}) or without FUS-IDR fusion (3×helix^{DRG9}). Scale bars, 5 μm.

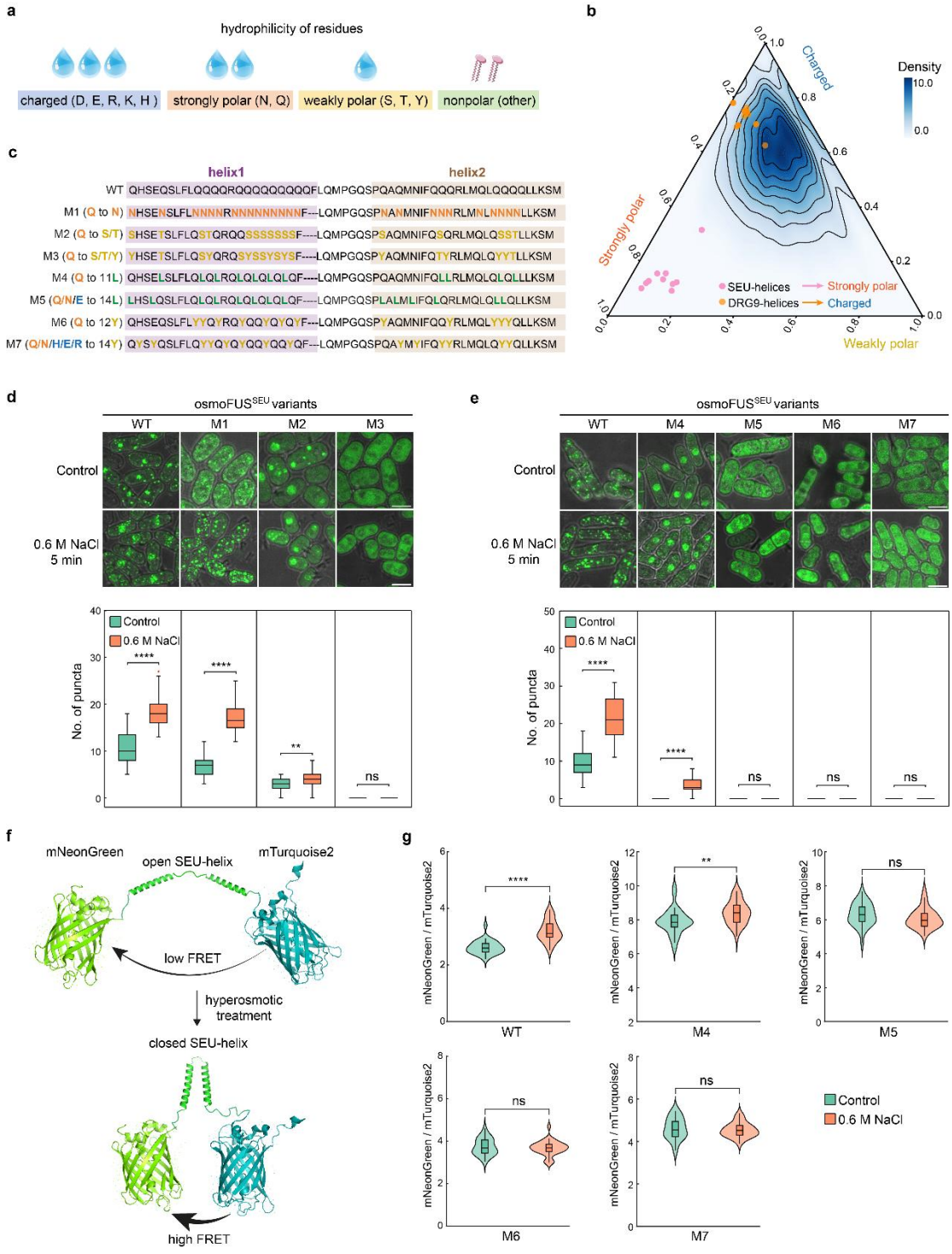

Fig. 2 Hydrophilicity contributes to hyperosmotic response of SEU-helix

(a) Four groups of amino acids with differential hydrophilicity. Charged and strongly polar residues have high hydrophilicity. Weakly polar residues have moderate hydrophilicity, while nonpolar residues are hydrophobic. D, Asp; E, Glu; R, Arg; K, Lys; H, His; Q, Gln; N, Asn; S, Ser; T, Thr; Y, Tyr.

(b) Ternary KDE (kernel density estimation) plot showing the distribution of residue composition of SEU- and DRG9-helices from representative plant taxa as in Supplementary Fig. 2 relative to the bulk control helices from PDB (Protein Data Bank). The three vertices correspond to charged (top), strongly polar (bottom left), and weakly polar residues (bottom right), respectively. SEU-helices clustered toward the strongly polar vertex, while DRG9-helices were shifted toward the charged-residue vertex, in contrast to the bulk control.

(c) Amino acid sequences of SEU-helix variants, with helix1 and helix2 indicating the left and right helices, respectively.

(d,e) Confocal images (top panels) and corresponding quantitative analyses (bottom panels) of yeast cells expressing mVenus-tagged osmoFUS^{SEU} (3×helix^{SEU}-FUS^{IDR}) variants as indicated in (c) under control or 0.6 M NaCl for 5 min. Box plots quantified puncta formation per cell. Each box encloses the middle 50% of the distribution, with the horizontal line marking the median and the vertical lines marking the minimum and maximum values that fall within 1.5 times the height of the box. ns, not significant; ****$p < 0.0001$, **$p < 0.01$ (Student's t test; $n \geq 30$ cells per group). Scale bars, 5 μm.

(f) Schematic diagram depicting FRET assay for probing conformational changes of a single SEU-helix.

(g) Violin plots quantifying FRET efficiency measured by mNeonGreen/mTurquoise2 fluorescence ratios for SEU-helix variants as indicated in (c) under control or 0.6 M NaCl. ns, not significant; ****$p < 0.0001$, ***$p < 0.001$, **$p < 0.01$, *$p < 0.05$ (Student's t test; $n \geq 30$ cells per group).

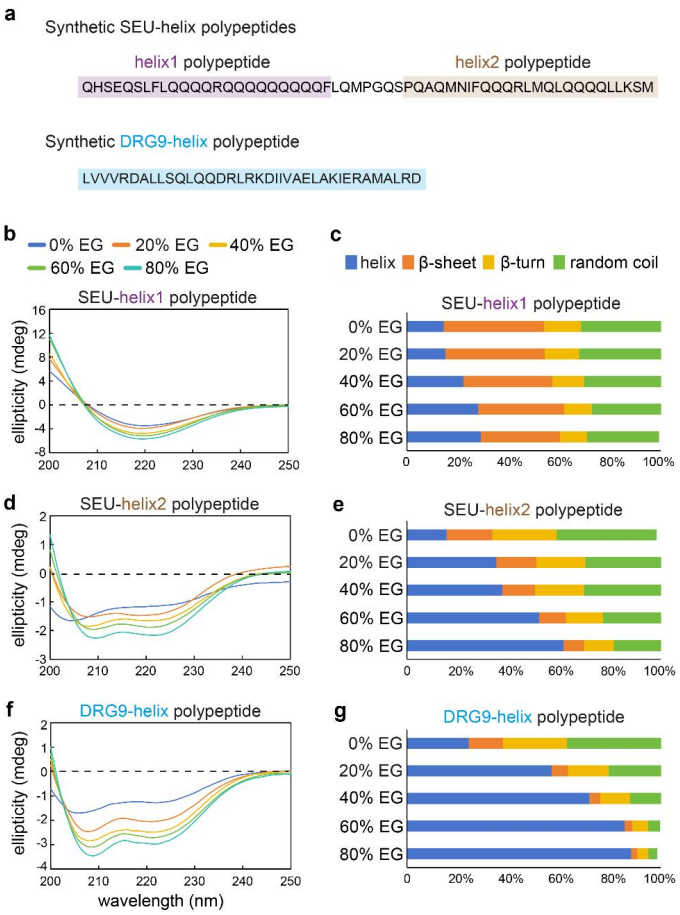

Fig. 3 Dehydration induces helix folding

(a) Amino acid sequences of synthetic SEU-helix1, SEU-helix2, and DRG9-helix.

(b,d,f) Circular dichroism (CD) spectra of synthetic SEU-helix1 (b), SEU-helix2 (d), and DRG9-helix (f) polypeptides. Ellipticity (mdeg) was plotted against wavelength (200-250 nm) at different ethylene glycol (EG) concentrations (0%, 20%, 40%, 60%, 80%).

(c,e,g) Secondary structure composition of synthetic SEU-helix1 (c), SEU-helix2 (e), and DRG9-helix (g) polypeptides. Stacked bar graphs showing fractions of α-helix (blue), β-sheet (orange), β-turn (yellow), and random coil (green) derived from CD spectra at corresponding EG concentrations.

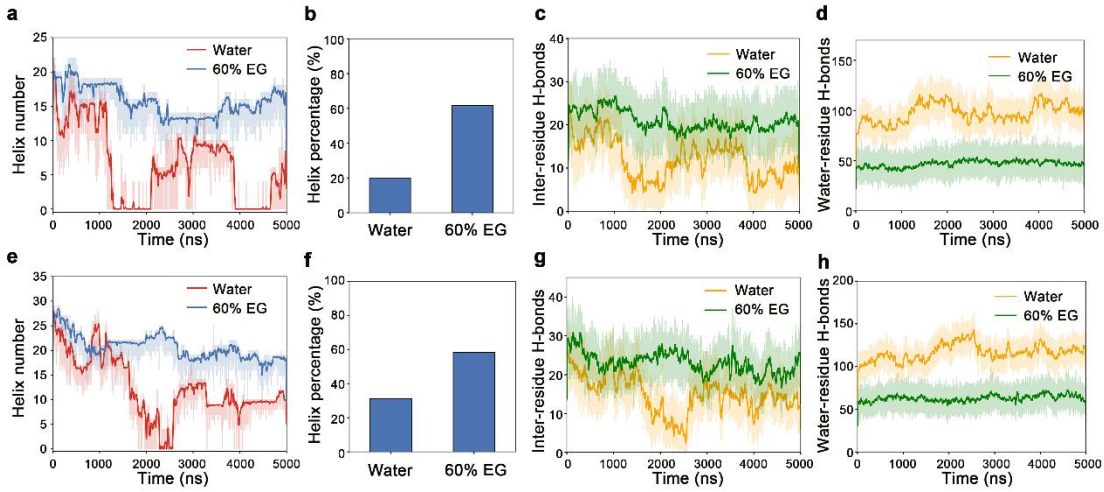

Fig. 4 Dehydration induces H-bonding alteration by MD simulations

(a) Time evolution simulation of helix number for SEU-helix1 in nanoseconds (ns).

(b) Average helix number of the last 2000-ns simulation for SEU-helix1 in water or 60% EG.

(c,d) Time evolution simulation of inter-residue (c) and water-residue H-bonds (d) for SEU-helix1 in nanoseconds (ns).

(e) Time evolution simulation of helix number for DRG9-helix in nanoseconds (ns).

(f) Average helix number of the last 2000-ns simulation for DRG9-helix in water or 60% EG.

(g,h) Time evolution simulation of inter-residue (g) and water-residue H-bonds (h) for DRG9-helix in nanoseconds (ns).

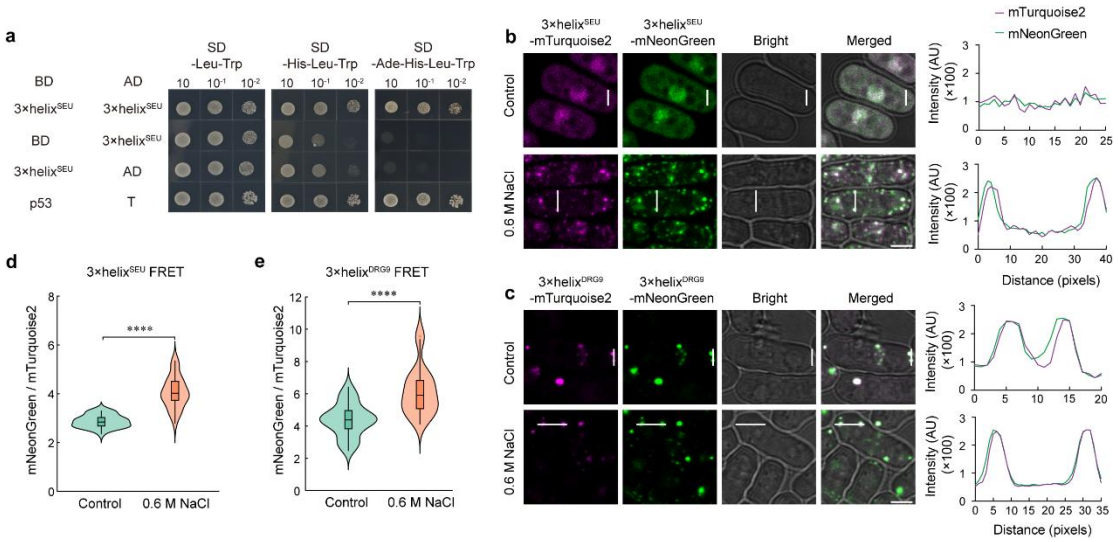

Fig. 5 Hyperosmolarity enhances intermolecular association of helices

(a) Yeast two-hybrid assay showing 3×helix^{SEU} self-association. BD and AD indicate DNA binding domain and activation domain of GAL4, respectively. BD-p53 and AD-T were used as positive control.

(b,c) Confocal images of yeast cells co-expressing 3×helix^{SEU}-mTurquoise2 and 3×helix^{SEU}-mNeonGreen (b), as well as 3×helix^{DRG9}-mTurquoise2 and 3×helix^{DRG9}-mNeonGreen (c) under control or hyperosmotic conditions (0.6 M NaCl, 5 min). The fluorescence intensities along the lines were shown in arbitrary units (AU) on the right. Scale bars, 5 μm.

(d,e) Violin plots quantifying FRET efficiency of intermolecular associations of 3×helix^{SEU} (d) and 3×helix^{DRG9} (e) under control or hyperosmotic conditions (0.6 M NaCl). ****$p < 0.0001$ (Student's t test, $n > 30$ cells per group).

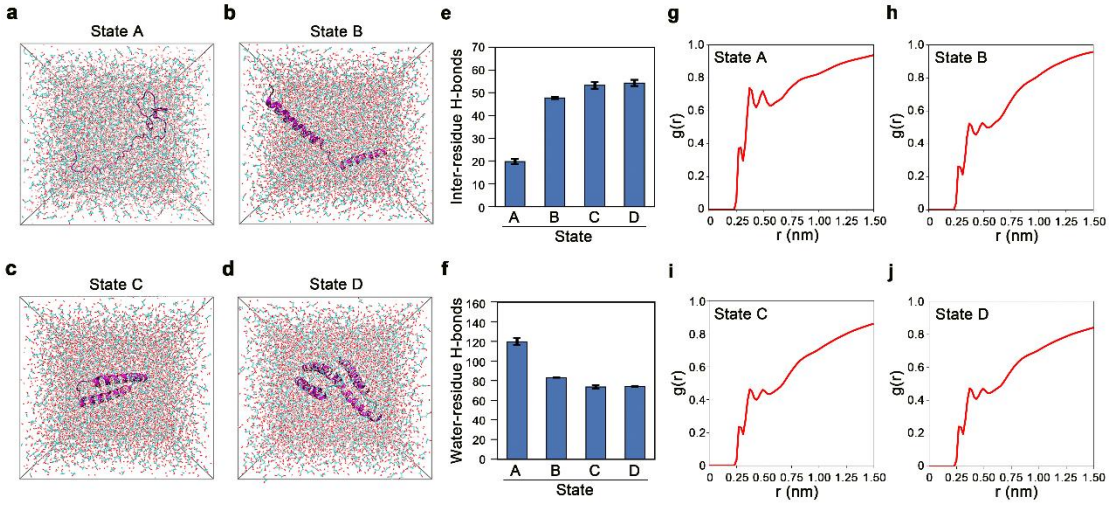

Fig. 6 Hydration analyses across distinct conformational states of SEU-helix by MD simulations

(a-d) Four typical conformations of SEU-helix in 60% EG from MD simulations.

(e,f) Average number of inter-residue (e) and water-residue (f) H-bonds.

(g-j) The radical distribution function (g(r)) of water molecules relative to proteins for the indicated States.

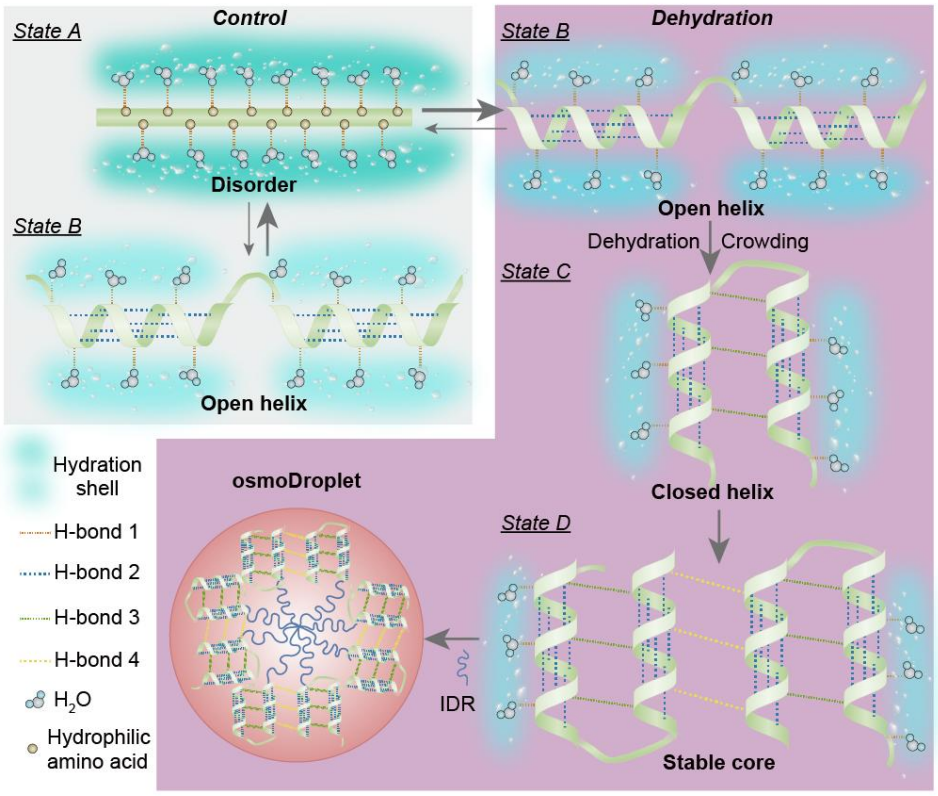

715

716 **Fig. 7 A model for osmoDroplet assembly**

717 Under control conditions, the metastable SEU-helix, which is enriched with highly
718 hydrophilic residues, tends to be unstructured with strong hydration shell maintained
719 by abundant residue-water hydrogen bonds (H-bond 1, *State A*). Hyperosmotic stress,
720 however, triggers a shift to *State B* (open helix) via dehydration, which reduces
721 residue-water H-bonds and hydration shell, and promotes residue-residue H-bonding
722 (H-bond 2). Subsequently, the open helix folds into a closed conformation (*State C*),
723 stabilized by inter-helix H-bonds (H-bond 3), likely through the combined effects of
724 dehydration and molecular crowding. Finally, the closed helices associate via
725 intermolecular H-bonds (H-bond 4) to form *State D*, creating a stable core that
726 nucleates the condensation of intrinsically disordered regions (IDRs) and drives
727 osmoDroplet assembly.

728

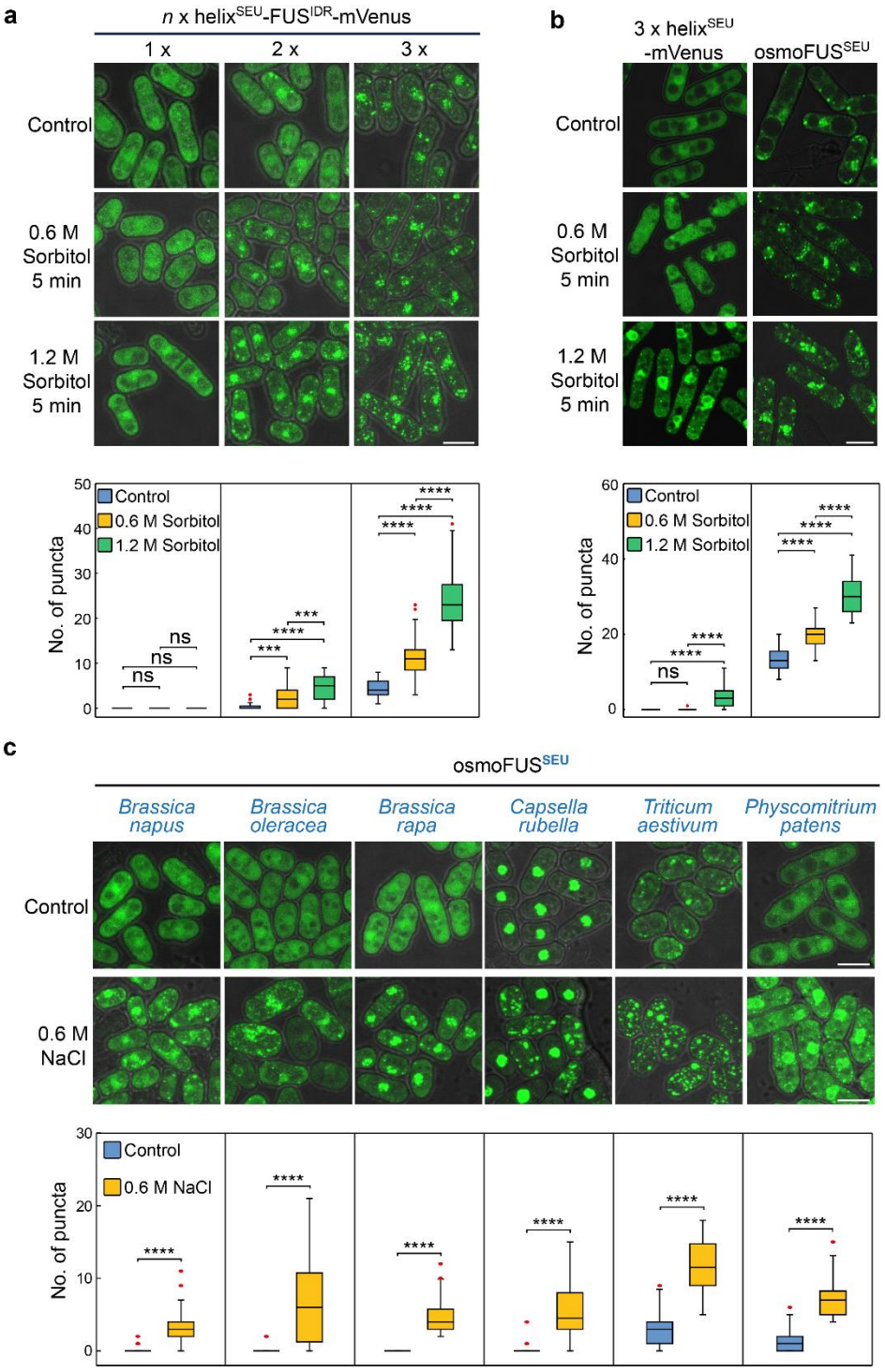

Fig. S1 Conserved helix-IDR osmoDroplet module

(a) Confocal images (top) and quantification (bottom) of yeast cells expressing *n*×helix^{SEU}-FUS^{IDR}-mVenus fusion proteins under control or sorbitol stress (0.6 M or 1.2 M, 5 min). Constructs vary by helix copy number (*n*=1, 2, 3). Box plots quantify puncta per cell.

(b) Confocal images (top) and quantification (bottom) of yeast cells expressing 3 copies of SEU-helices with (osmoFUS^{SEU}) or without FUS-IDR fusion (3×helix^{SEU}) under control and sorbitol-stress conditions (0.6 M or 1.2 M, 5 min).

(c) Confocal images (top) and quantification (bottom) of yeast cells expressing 3 copies of SEU-helices with FUS-IDR fusion (osmoFUS^{SEU}), with SEU-helices from the indicated plant taxa: *Brassica napus, Brassica oleracea*, *Brassica rapa*, *Capsella rubella*, *Triticum aestivum*, *Physcomitrium patens* under control and 0.6 M NaCl (5 min) conditions.

(a-c) Box plots quantifying puncta formation per cell. Each box encloses the middle 50% of the distribution, with the horizontal line marking the median and the vertical lines marking the minimum and maximum values that fall within 1.5 times the height of the box. ns, not significant; ****$p < 0.0001$, ***$p < 0.001$ (one-way ANOVA followed by Tukey's HSD test for (a,b) and Student's *t* test for (c); $n \geq 30$ cells per group). Scale bars, 5 μm.

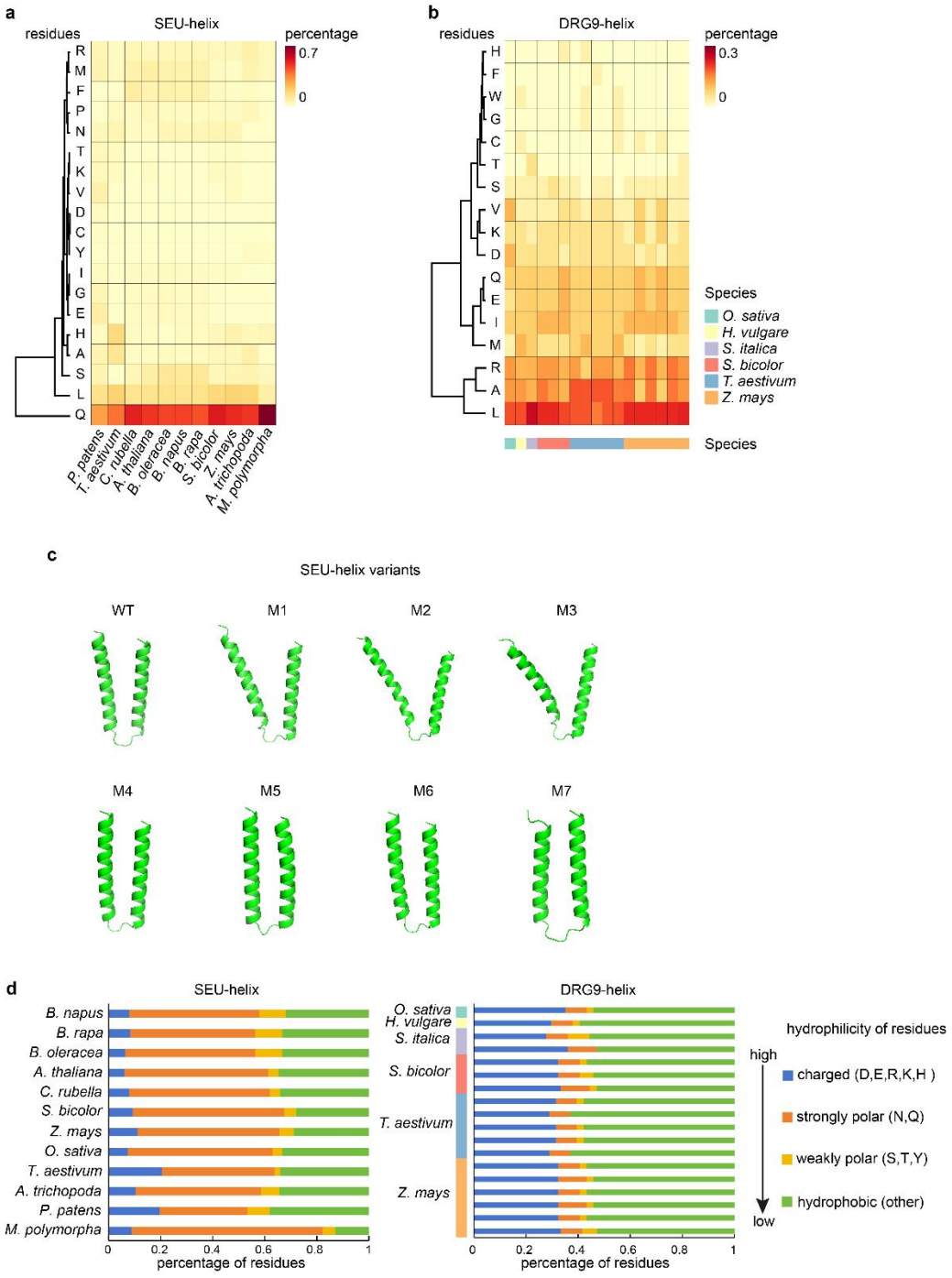

Fig. S2 Sequence and structure analyses of SEU/DRG9-helix and the variants

(a,b) Heatmap clustering analysis showing enrichment of individual residues in SEU-helices (a) and DRG9-helices (b) from the indicated plant taxa.

(c) AlphaFold3 predictions of SEU-helix variants corresponding to Fig. 2c.

(d) Sequence composition of SEU- and DRG9-helices from the indicated plant taxa. Residues were grouped into four types according to hydrophilicity.

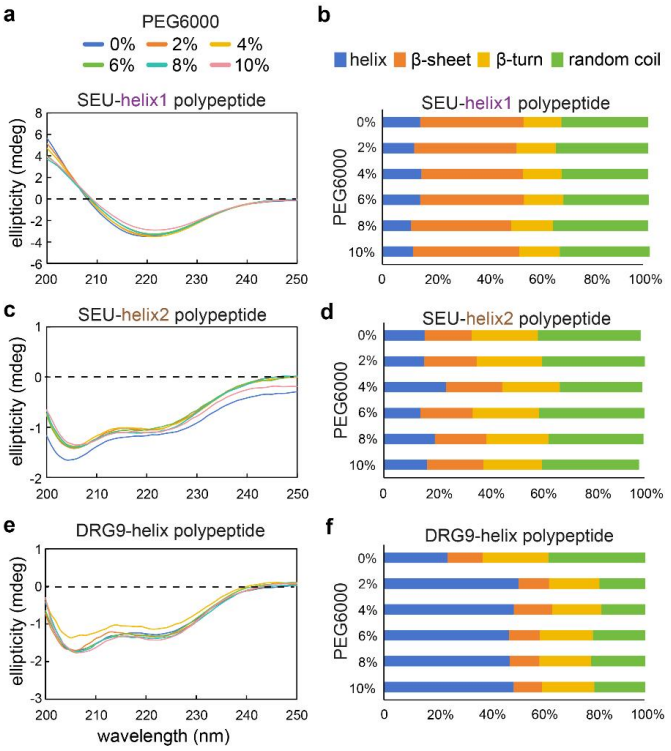

Fig. S3 Molecular crowding induces marginal helix folding

(a,c,e) Circular dichroism (CD) spectra of synthetic SEU-helix1 (a), SEU-helix2 (c), and DRG9-helix (e) polypeptides. Ellipticity (mdeg) was plotted against wavelength (200-250 nm) at different polyethylene glycol (PEG6000) concentrations (0%, 2%, 4%, 6%, 8%, 10%).

(b,d,f) Secondary structure composition of synthetic SEU-helix1 (b), SEU-helix2 (d), and DRG9-helix (f) polypeptides. Stacked bar graphs showing fractions of α-helix (blue), β-sheet (orange), β-turn (yellow), and random coil (green) derived from CD spectra at corresponding PEG concentrations.

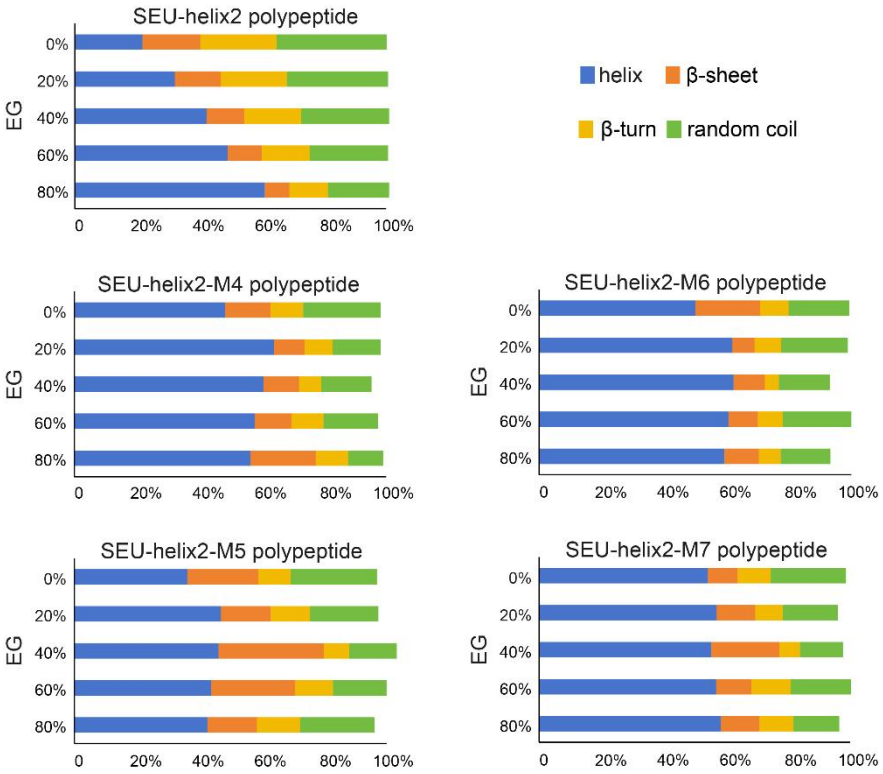

769

770 **Fig. S4 High hydrophilicity is essential for helix transition under EG**

771 Secondary structure composition of synthetic polypeptides of SEU-helix2 and its
772 variants corresponding to M4-M7 as depicted in Fig. 2c. Stacked bar graphs showing
773 fractions of α-helix (blue), β-sheet (orange), β-turn (yellow), and random coil (green)
774 derived from CD spectra at corresponding EG concentrations.

775

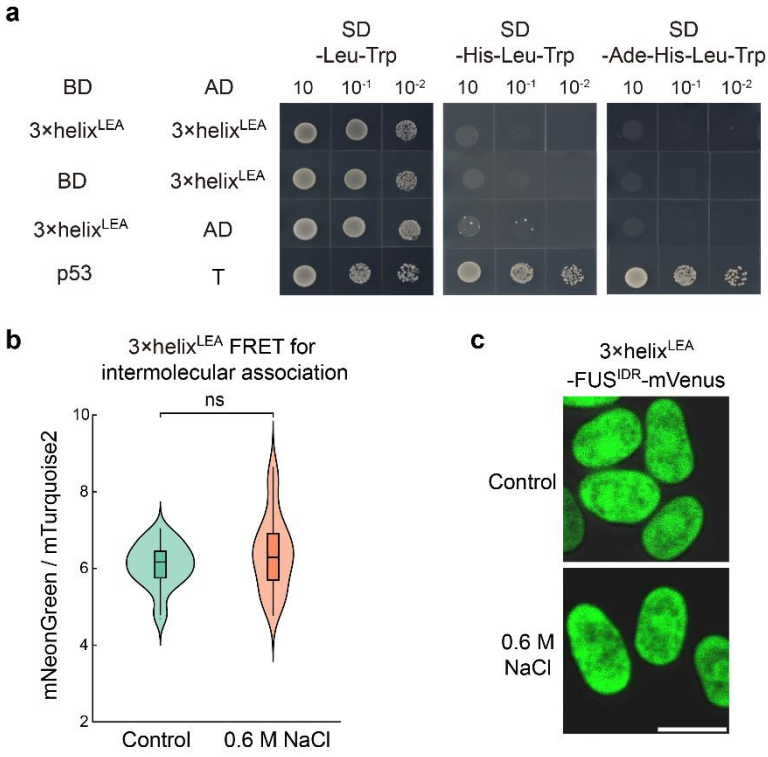

Fig. S5 LEA helix fails to self-interact or drive condensation

(a) Yeast two-hybrid assay of 3xhelix^{LEA}. BD and AD indicate DNA binding domain and activation domain of GAL4. BD-p53 and AD-T were used as positive control.

(b) Violin plots quantifying FRET efficiency of intermolecular associations of 3xhelix^{LEA} under control or hyperosmotic conditions (0.6 M NaCl). ns, not significant (Student's *t* test, *n* >30 cells per group).

(c) Confocal images of yeast cells expressing 3×helix^{LEA}-FUS^{IDR}-mVenus under control or hyperosmotic conditions (0.6 M NaCl, 5 min).

Supplementary Movies 1-4. Time evolution simulations of SEU-helix1 in EG (Movie 1), water (Movie 2), and of DRG9-helix in EG (Movie 3), water (Movie 4) within 5000 nanoseconds (ns).